Mineralium Deposita (2002) 37: 599–613
DOI 10.1007/s00126-002-0270-y

ARTICLE

Kalin Kouzmanov · Laurent Bailly
Claire Ramboz · Olivier Rouer · Jean-Michel Bény

Morphology, origin and infrared microthermometry of fluid inclusions in pyrite from the Radka epithermal copper deposit, Srednogorie zone, Bulgaria

Received: 7 February 2001 / Accepted: 19 December 2001 / Published online: 12 April 2002

Abstract Pyrite samples from the Radka epithermal, replacement type, volcanic rock-hosted copper deposit, Bulgaria, have been studied using near-infrared (IR) microscopy. Two generations of pyrite based on their textures, composition and behaviour in IR light can be distinguished. Electron microprobe analyses, X-ray elemental mapping and Fourier transform infrared spectroscopy were used to study the relationship between crystal zoning, trace element contents and IR transmittance of pyrite. The observed crystal zoning is related to variable arsenic contents in massive fine-grained and colloform pyrite from the early pyrite–quartz assemblage, and cobalt contents in pyrite crystals from the late quartz–pyrite vein assemblage. There is a negative correlation between trace element content and IR transmittance of pyrite. The IR transparency of pyrite is thus a sensitive indicator of changes in trace element concentrations. Fluid inclusions have only been found in the second pyrite generation. Scanning electron microscopy observations on open fluid inclusion cavities permitted the crystallographic features of vacuoles to be determined. A characteristic feature of primary fluid inclusions in pyrite is a negative crystal habit, shaped mainly by {100}, {111} and {210}. This complicated polyhedral morphology is the reason for the observed opacity of some isometric primary inclusions. Secondary fluid inclusion morphology depends on the nature of the surface of the healed fracture. Recognition of the primary or secondary origin of fluid inclusions is enhanced by using crystallographically oriented sections. Microthermometric measurements of primary inclusions indicate that the second pyrite generation was deposited at maximum P–T conditions of 400 °C and 430 bar and from a fluid of low bulk salinity (3.5–4.6 wt%), possibly KCl-dominant. There are large ranges for homogenisation temperatures in secondary inclusions because of necking-down processes. Decrepitation features of some of pyrite-hosted inclusions and of all inclusions in associated quartz indicate reheating of the veins to 500–550 °C. The late cobalt-rich quartz–pyrite vein assemblage in the Radka deposit may be the shallow manifestation of deeper and genetically related porphyry copper mineralisation. This is a common observation of many intermediate- to high-sulfidation epithermal replacement-type ore bodies in this ore district and possibly the Cretaceous Banat–Srednogorie metallogenic belt in general.

Keywords Bulgaria · Epithermal · Fluid inclusions · Infrared microthermometry · Pyrite · Srednogorie zone

K. Kouzmanov (✉)
Institut des Sciences de la Terre d'Orléans (ISTO) – CNRS,
1A rue de la Férollerie, 45071 Orléans cedex 2, France
E-mail: kouzmanov@erdw.ethz.ch
Fax: +41-1-6321827

K. Kouzmanov
Sofia University, Dept. of Mineralogy,
Petrology and Economic Geology,
15, Tsar Osvoboditel Bd, 1000 Sofia, Bulgaria

L. Bailly
BRGM, REM/MESY, BP 6009,
45060 Orléans cedex 2, France

C. Ramboz · O. Rouer · J.-M. Bény
Institut des Sciences de la Terre d'Orléans (ISTO) – CNRS,
1A rue de la Férollerie, 45071 Orléans cedex 2, France

Present address: K. Kouzmanov
Isotope Geochemistry and Mineral Resources,
Department of Earth Sciences, ETH Zürich, Switzerland

Introduction

Pyrite is the most common and widespread sulphide mineral in nature and occurs as a major component in many types of hydrothermal ore deposits. Numerous investigations have demonstrated the wide variety of morphological, textural, compositional, paragenetic and isotopic variations of pyrite of different origins. Its internal and textural features are studied mainly using reflected light microscopy, sometimes coupled with other techniques such as chemical etching (e.g. Ramdohr 1981; Fleet et al. 1989), colour staining and surface oxidation

(Fleet et al. 1993), backscattered electron imaging (e.g. Fleet and Mumin 1997; Craig et al. 1998) and secondary ion mass spectrometry (SIMS) mass-specific mapping (Simon et al. 1999).

Infrared (IR) transmitted-light microscopy provides the means to observe internal textures and structures of some ore minerals that are opaque to visible light, but transparent to IR radiation (Campbell et al. 1984). Campbell and Robinson-Cook (1987) demonstrated the application of this technique to the study of fluid inclusions in such minerals in combination with microthermometric analyses. Since then, several studies of fluid inclusions in different opaque minerals have been performed, including wolframite (Campbell et al. 1988; Campbell and Panter 1990; Lüders 1996), enargite (Mancano and Campbell 1995), stibnite (Lüders 1996; Bailly et al. 2000), hematite and hausmannite (Lüders et al. 1999).

The first study of pyrite using an IR transmitted-light microscope was conducted by Richards and Kerrich (1993). They observed growth zoning of pyrite caused by variable arsenic contents, and fluid and solid inclusions parallel to the growth bands. Their scanning electron microscopy (SEM) study of decrepitated fluid inclusions revealed the presence of Cl, Ca and Na, and minor K in decrepitation residue deposited on the surface of pyrite. Microthermometric data were not reported in their paper. Mancano and Campbell (1995) provided the first freezing measurements on fluid inclusions hosted by pyrite. Lüders and Ziemann (1999) recently demonstrated the possibilities and the limitations of IR-microthermometry applied to pyrite-hosted fluid inclusions. Their study, based on a detailed investigation of pyrite samples from various mineral occurrences and of different origins, emphasised the restricted applicability of the IR-microthermometry to this mineral. Their conclusions are based on a limited number of samples transparent to IR light and containing fluid inclusions suitable for microthermometric measurements. Lüders and Ziemann (1999) also noted that samples commonly become completely opaque during heating before the homogenisation temperature is reached. In spite of these difficulties, some homogenisation (Th = 229–307 °C) and cryometric measurements (eutectic and melting points) were performed on samples from the Murgul copper deposit, Turkey. Kulis and Campbell (1999) studied the near-infrared transparency of cobalt-bearing pyrite from various localities. They analysed pyrite by means of infrared microscopy, Fourier transform infrared (FTIR) spectroscopy, bulk geochemical and electron-microprobe analyses, and found an excellent negative correlation between the concentration of cobalt and IR transparency.

In this paper, we report the results of a systematic investigation of pyrite-hosted fluid inclusions from the Radka copper deposit, Srednogorie zone, Bulgaria. Fluid inclusions in single pyrite crystals and massive fine-grained and colloform aggregates were studied using near IR microscopy. Combined electron-probe microanalyses (EPMA), X-ray elemental mapping and FTIR spectroscopy were used to establish the relationship among crystal zoning, trace element distribution and IR transmittance of pyrite. Also, SEM observations on open fluid inclusion cavities permitted the crystallographic features of vacuoles with negative crystal shapes to be determined. Finally, we discuss the genetic implications of the microthermometric data from the pyrite-hosted fluid inclusions.

Geological setting and conditions of ore formation

The Radka deposit is located in the south-eastern part of the Panagyurishte district, in the central part of the Srednogorie metallogenic zone (Fig. 1). The district is composed of Precambrian(?) gneisses, Palaeozoic granites and a Late Cretaceous volcano–plutonic complex (Fig. 1). In some parts of the district, these rocks are covered by Maestrichtian flyschoid sedimentary rocks and small outcrops of Palaeogene and Neogene molasse (Bogdanov 1980). Late Cretaceous magmatic activity, calc-alkaline to subalkaline in composition, is closely related to two main types of ore deposits: massive Cu–S ± Ag–Au deposits of replacement origin (Krassen, Radka and Elshitsa) and porphyry copper deposits (Assarel, Petelovo, Tsar Assen, Vlaykov Vruh and Popovo Dere – Fig. 1b; Bogdanov 1980).

Two hypotheses have been proposed for ore formation in the district. Dimitrov (1960) defined the volcanic rock-hosted Cu–S ± Ag–Au mineralisation as "replacement type meso- to epithermal in nature". This is because Late Cretaceous andesite and dacite volcanic rocks form, because of their high permeability, a favourable environment for metasomatic replacement and hydrothermal mineral precipitation. Further, considering the fact that both the rhyodacite dykes and the subvolcanic granodiorites host a Cu–Mo mineralisation, this author proposed that the rhyodacite dykes were subsurface analogues of the deep granodiorite intrusions (see Fig. 1d). Dimitrov (1960) also suggested that the massive Cu–S ± Au–Ag mineralisation was genetically related to these felsic magmatic rocks. By contrast, Bogdanov (1980, 1984) considered that the massive pyrite bodies were volcanic-hosted massive sulphide (VMS) deposits, formed on the sea floor. The late copper-pyrite ore bodies replaced pyritic bodies because of late copper-enriched hydrothermal fluid circulation originating from the post-volcanic rhyodacite dykes. According to Bogdanov (1980, 1984), there is no genetic connection

Fig. 1 **a** Position of the Srednogorie zone and the Panagyurishte district. *Rectangle* shows the area enlarged in **b**. **b** Geology of the Panagyurishte district with location of the major mineral occurrences (modified from Bogdanov 1980). **c** Simplified geological map of the Radka deposit (modified from Obretenov and Popov 1973). **d** Cross section of the Radka deposit (after Popov and Popov 1997; Tsonev et al. 2000b)

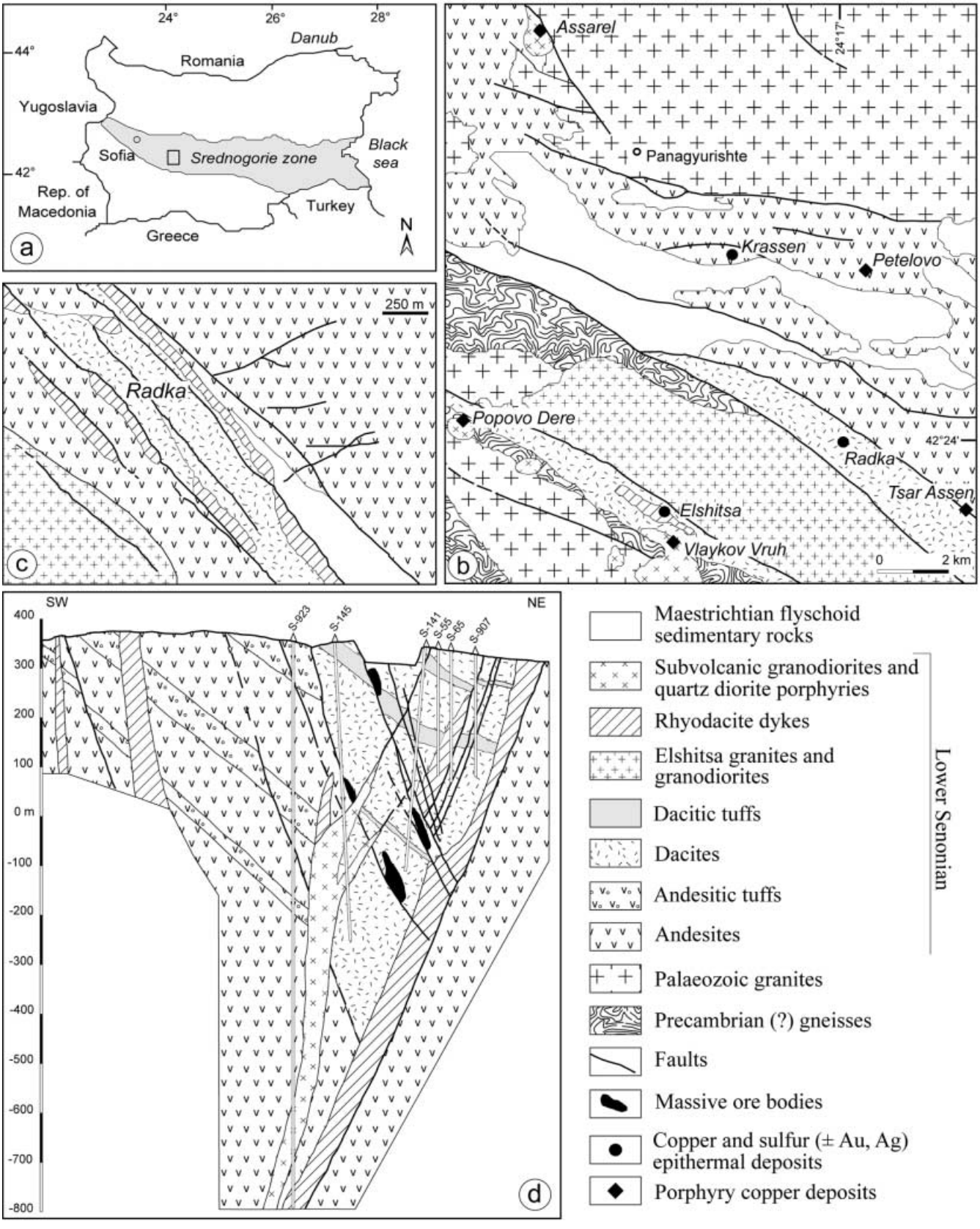
24°
26°
28°
44°
42°
Danub
Romania
Yugoslavia
Sofia
Srednogorie zone
Black sea
Rep. of Macedonia
Turkey
Greece
N
a
Assarel
24°17'
Panagyurishte
Krassen
Petelovo
Popovo Dere
42°24'
Radka
Tsar Assen
Elshitsa
Vlaykov Vruh
0
2 km
b
250 m
Radka
c
SW
NE
S-923
S-145
S-141
S-55
S-65
S-907
400
300
200
100
0 m
-100
-200
-300
-400
-500
-600
-700
-800
d
Maestrichtian flyschoid sedimentary rocks
Subvolcanic granodiorites and quartz diorite porphyries
Rhyodacite dykes
Elshitsa granites and granodiorites
Dacitic tuffs
Dacites
Andesitic tuffs
Andesites
Lower Senonian
Palaeozoic granites
Precambrian (?) gneisses
Faults
Massive ore bodies
Copper and sulfur (± Au, Ag) epithermal deposits
Porphyry copper deposits

between the formation of VMS deposits and the porphyry copper mineralisation. Recently, Tsonev et al. (2000a), in agreement with the original epigenetic theory of Dimitrov (1960) and consistent with present genetic models of ore formation in the porphyry/epithermal environment (Hedenquist and Lowenstern 1994; Hedenquist and Arribas 1999; Hedenquist 2000), defined the Radka deposit as a transitional epithermal system with an intermediate sulphidation (IS) style of mineralisation. Recent data from the southern part of the Panagyurishte district confirm that both plutonic and subvolcanic rocks have a similar lead isotopic signature, which is identical to that of both types of ores (Kouzmanov et al. 2001).

The Radka copper deposit is one of the largest deposits in the Panagyurishte ore district, a district that also hosts the world-class Au–Cu deposit of Chelopech that is located 30 km north-north-west of Radka (Andrew 1997, Bonev et al. 2002, this volume). Production from the Radka deposit during 1942–1995 was 6.39 million tons (t) of copper ore grading 1.06% Cu, and 0.28 million t of pyrite ore grading 28.6% S, with a total production of 68,006 t of copper and 78,954 t of sulphur (Milev et al. 1996). Gold and silver were extracted as a by-product from the pyrite and copper concentrate. The mine closed in 1995. The deposit consists of several steeply dipping, lenticular massive ore bodies with a halo of veinlets and disseminated ores. Ore is confined to fault zones striking west-north-west and is hosted by felsic volcanic rocks (dacite lavas, tuffs and tuff breccias), crosscut by rhyodacite dykes (Fig. 1c, d; Dimitrov 1960).

The main minerals in the massive ores at the Radka deposit are pyrite, chalcopyrite, bornite, tennantite, enargite, sphalerite, galena and chalcocite. Numerous subordinate and rare Ge-, Ga-, In-, Sn-, Bi- and Te-bearing minerals are also present (Tzonev 1982; Kouzmanov et al. 2000a). Late anhydrite is abundant in the upper part of the deposit. According to Bogdanov and Bogdanova (1974) and Tzonev (1974), the mineral paragenesis consists of (1) early pyrite–quartz, (2) chalcopyrite–pyrite, (3) enargite–pyrite, (4) bornite–tennantite, (5) sphalerite–galena, (6) late quartz–pyrite, (7) pyrite–marcasite and (8) anhydrite–gypsum. Wall rock alteration is structurally and morphologically related to ore-controlling faults. Radonova (1962) and Chipchakova et al. (1981) described outward zonation of alteration from the ore bodies consisting of quartz–sericite, quartz–chlorite–sericite and propylitic assemblages.

Limited fluid inclusion data for the Radka deposit are available in Strashimirov and Kovachev (1992). They report 225–245 °C for the homogenisation temperature (Th) of inclusions in quartz from the early pyrite–quartz assemblage, and Th temperatures between 180 and 230 °C in late anhydrite. Kouzmanov et al. (2000b) performed an extensive study of quartz-hosted, primary fluid inclusions from the main chalcopyrite–pyrite stage. They identified, by micro-Raman spectrometry, trapped kaolinite and sericite in these inclusions and CO_2, $H_2 \pm N_2$ in the volatile phase. Microthermometric measurements indicated salinities ranging from 2.4 to 3.4 wt% equiv. NaCl with a mean of 2.8 ± 0.3 wt% equiv. NaCl. The inclusions homogenised to the liquid between 218 and 260 °C, with a mode at 250 °C. The presence of two hydrothermal alumino-silicates in these primary fluid inclusions indicates that they contain a mildly acidic fluid with a pH of about 4 at 250 °C (Heald et al., 1987). In the context of a replacement epithermal deposit, these volatile-rich acidic inclusion fluids could contain a magma-derived component (e.g. Herzig et al. 1998). At the Elshitsa deposit, where quartz-hosted, sericite-bearing, aqueous inclusions are also present, stable isotope studies (O, H, S) implicate a magmatic fluid component (Kouzmanov and Lerouge, unpublished data).

Samples and analytical techniques

Single pyrite crystals and massive fine-grained and colloform pyrite aggregates were studied. Single crystals were extracted from the late quartz–pyrite veins cutting the dacite lavas, tuffs and breccias, and surrounded by quartz–sericite alteration (Fig. 2a). The veins are 2 to 15 cm wide and are composed of euhedral pyrite crystals (3–15 mm in size; Fig. 2b), bounded mainly by *a* {100} and *o* {111}, and massive and euhedral quartz with individual crystals as long as 10 mm (Fig. 2b). This late mineral assemblage lacks ore grade material. Small tetrahedral crystals of chalcopyrite, as much as 2 mm in diameter, are rare. Two samples of massive pyrite associated with the early pyrite–quartz assemblage, forming the massive pyrite ore bodies, have also been studied.

Twenty-five doubly polished oriented crystal sections (100–150 μm in thickness), cut parallel to (100) and (111), were used in this study. Fluid inclusions were studied on a US Geological Survey-type microthermometric stage mounted on an Olympus BHMS microscope equipped for IR-microscopy ($\lambda \leq 2.5$ μm; Bailly 1998) at BRGM. Transmission spectra of individual pyrite crystals in the near IR region were collected using a Nicolet Magna-IR 760 FTIR spectrometer (20-μm aperture) at ISTO-CNRS. EPMA and X-ray elemental mapping were performed at BRGM using a CAMECA SX 50 electron-microprobe with PAP correction program (Pouchou and Pichoir 1984). Operating conditions were accelerating voltage at 25 kV, beam current at 60 nA and beam diameter at 1 μm. Pyrite, GaAs, Sb_2S_3, Cu, Ni, Co, Se, Au and Ag were used as standards for calibration. Counting times for major (Fe, S) and trace elements were 10 and 40 s, respectively. Carbon-coated samples of polished (100) sections with open fluid inclusion cavities were examined with a JEOL 6400 scanning electron microscope at the ESEM – University of Orléans, in order to determine the crystallographic morphology of the vacuoles. The SEM images were interpreted by comparison with oriented crystal

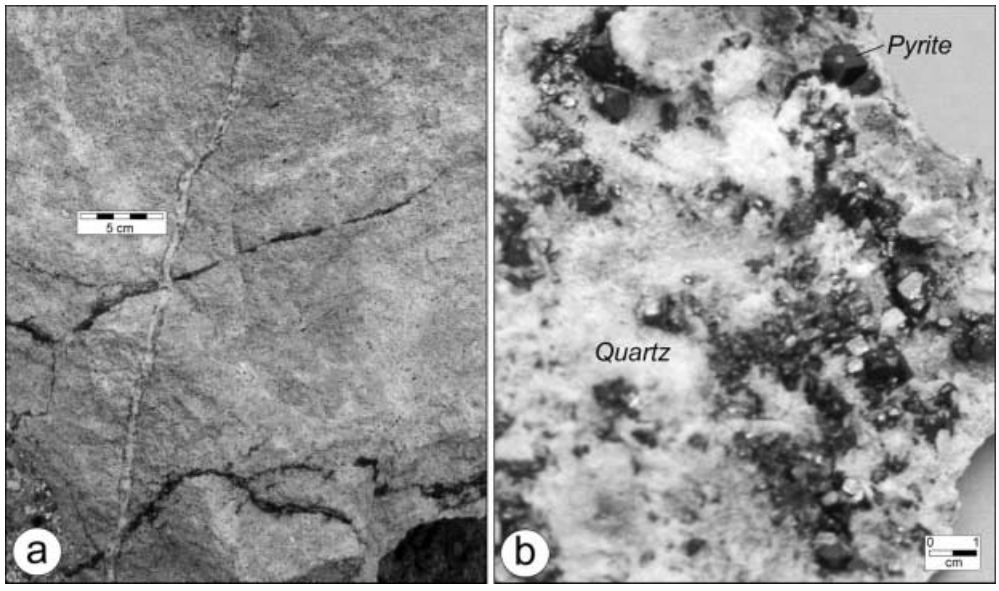

Fig. 2 **a** Late quartz–pyrite veins, cutting the early pyrite–quartz assemblage. **b** Euhedral pyrite crystals intergrown with quartz

projections simulated using the SHAPE program of Dowty (1989).

Results

Pyrite zoning

Two pyrite generations have been recognised in the Radka deposit. These are distinguished based on structure, texture, composition and IR-light behaviour.

Fine-grained and colloform pyrite from the early pyrite–quartz assemblage shows visible zoning in reflected light, even before etching with HNO_3. The backscattered electron (BSE) images and EPMA show that this fine oscillatory growth zoning is caused by the presence of as much as 2.2 wt% As. No other trace elements were detected, except for 800–1,200 ppm Cu in three analyses and 300 ppm Sb in one sample. In IR transmitted light, this generation of pyrite is completely opaque, except for very fine growth bands in some crystals (3–4 μm in width), which probably have no or very little arsenic. The exact arsenic content of these zones could not be determined because they are smaller than or equivalent to the beam size of the microprobe. No fluid inclusions were observed in massive pyrite.

No crystal zoning was observed in pyrite crystals from the late quartz–pyrite vein assemblage using reflected light microscopy. Isolated inclusions of chalcopyrite, sphalerite and galena are present and, in some cases, can be parallel to crystal faces. In two crystals, some cracks are filled with marcasite and recrystallised pyrite from the relatively late pyrite–marcasite assemblage. Intimate intergrowth textures of pyrite and quartz are common. All pyrite crystals show very good IR transmittance and spectacular crystal zoning (Fig. 3a). A general rule for the evolution of zoning is the development of {111} in the crystal core followed by {100} towards the rim (Fig. 3b, c). Both cubic and octahedral growth bands show very fine and locally very complicated structures. In some cases, (100) faces are stepped by the presence of {210}, {111} and/or vicinal-like forms (Fig. 3d). This stepped structure of the cubic growth zones is outlined by different IR transmittance. The growth zoning in pyrite is rarely marked by the presence of solid inclusions, probably clay minerals.

The X-ray elemental mapping (Fig. 4) and EPMA were performed in order to determine the nature of the observed zoning. Cobalt was the only trace element detected in significant and variable amounts in the different zones. X-ray mapping revealed a zonal distribution of cobalt in crystal cores (Fig. 4a), although this zonal distribution was not detectable by individual spot microprobe analyses. The concentration of cobalt in the centre of a typical crystal (the brighter triangular area in Fig. 4a, presumably corresponding to slightly higher cobalt-content), and immediately next to the centre, is about 0.02–0.08 wt% Co. The crystal rims are cobalt-enriched (white bands on Fig. 4a), with as much as 1.9 wt% Co, and show an oscillatory zoned cobalt distribution. No nickel and arsenic were detected by both X-ray elemental mapping (Fig. 4b, c) and EPMA.

To determine the relationship between IR-transparency and crystal zoning in pyrite, IR spectra of selected areas with contrasting composition and behaviour in IR light were obtained (Fig. 3a, b). The area bordering the inner triangular zone shows an excellent IR-transmittance (as much as 95%), whereas the triangle itself shows a transmittance below 17%. In areas where oblique secondary inclusion planes are present, the IR transmittance decreases a further 10%. The cobalt-rich rim of the studied crystal is completely opaque to IR light.

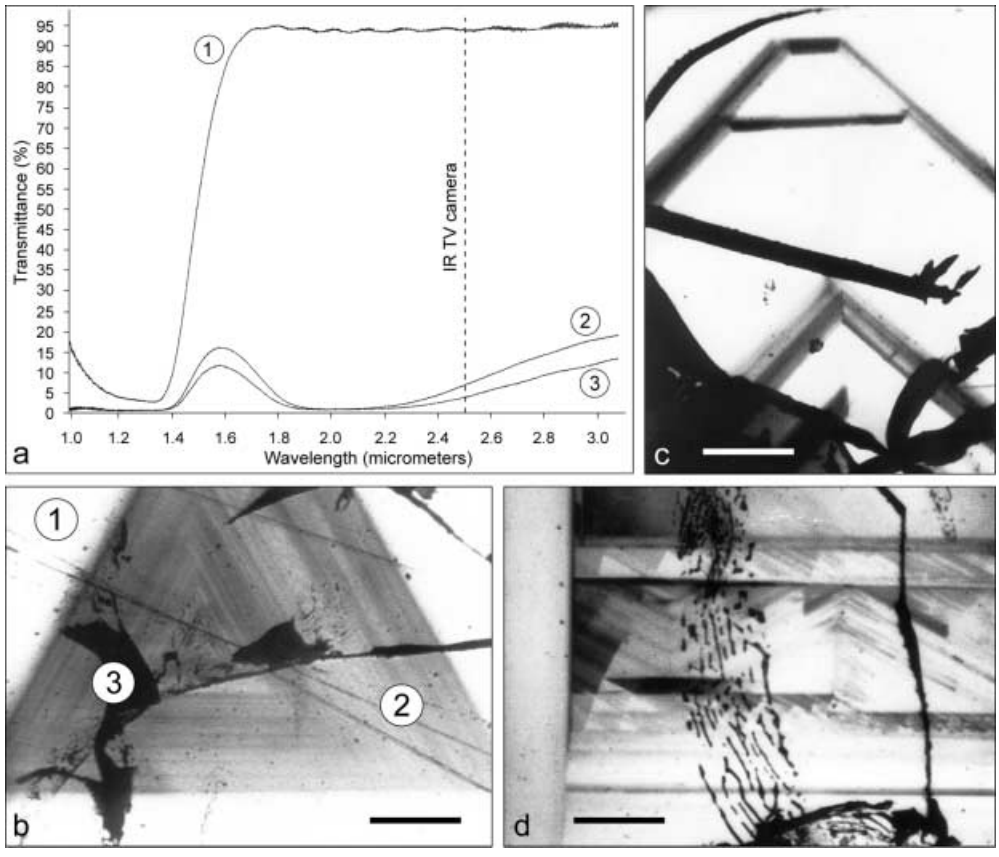

Fig. 3 **a** FTIR spectra of zoned pyrite crystal. Locations of different spectra are shown on **b**. **b** IR transmitted light microphotograph of zoned pyrite crystal cut parallel to (111). Locations of areas where FTIR spectra were performed are shown by 1, 2 and 3. **c**, **d** IR transmitted light microphotographs of zoned pyrite crystal cut parallel to (100). **c** Crystal zoning caused by variable cobalt-content marks conversions of crystal habit of pyrite. **d** Stepped zoning of (100) growth bands, resulting from the presence of {210}, {111} and/or vicinal-like forms. *Scale bar* 80 μm

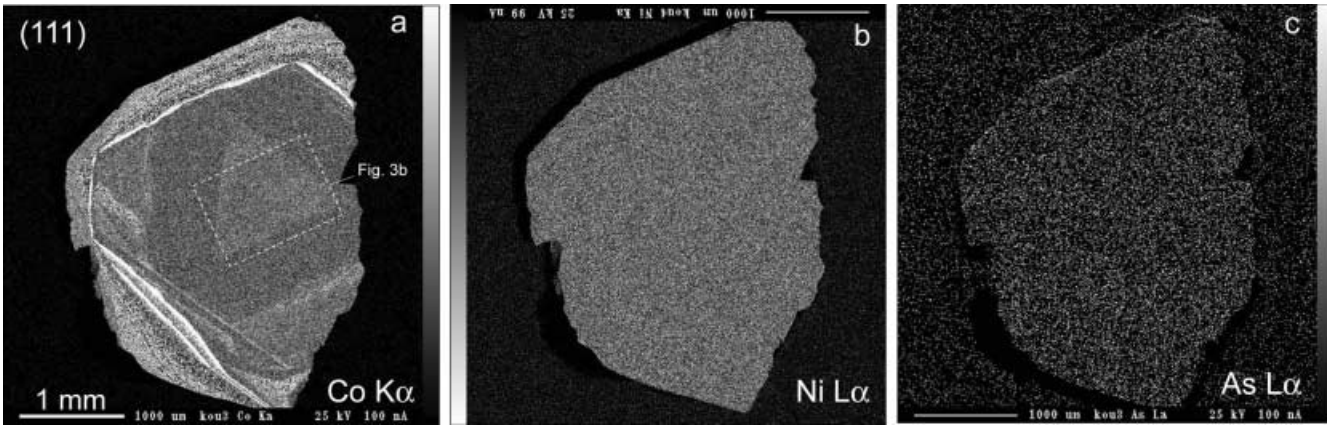

Fig. 4a–c X-ray elemental mapping of zoned pyrite crystal cut parallel to (111). **a** Cobalt distribution. Note the *small triangle* in the centre of the crystal, corresponding to Fig. 3b. **b** Nickel distribution. **c** Arsenic distribution

Morphology and origin of fluid inclusions in pyrite

Two types of fluid inclusions have been distinguished according to their morphology and position inside euhedral pyrite crystals. These are defined as primary and secondary inclusions.

Primary inclusions (Fig. 5) are arranged along growth zones in the <100> growth pyramids or are situated in the crystal cores. They are two-phase liquid–vapour, with a degree of fill of about 0.50–0.60. The inclusion cavities are negative crystals (Fig. 5a–c), bounded in general by the most important pyrite forms: *a* {100}, *o* {111} and *e* {210}. In addition, small faces of *n* {112}, *s* {321} and two other {hkl} forms are identified. Primary inclusions display three types of morphologies, which are described below.

Elongated channel-like inclusions (Fig. 5a), parallel to the growth zones, are bounded by *a*, *o* and *e*, with preferential development of cubic faces. The inclusions are strongly anisometric, and as much as 400 μm long and 100 μm wide.

Nearly isometric inclusions (Fig. 5b, c) exhibit more complicated morphologies. The *a*, *o* and *e* faces in these

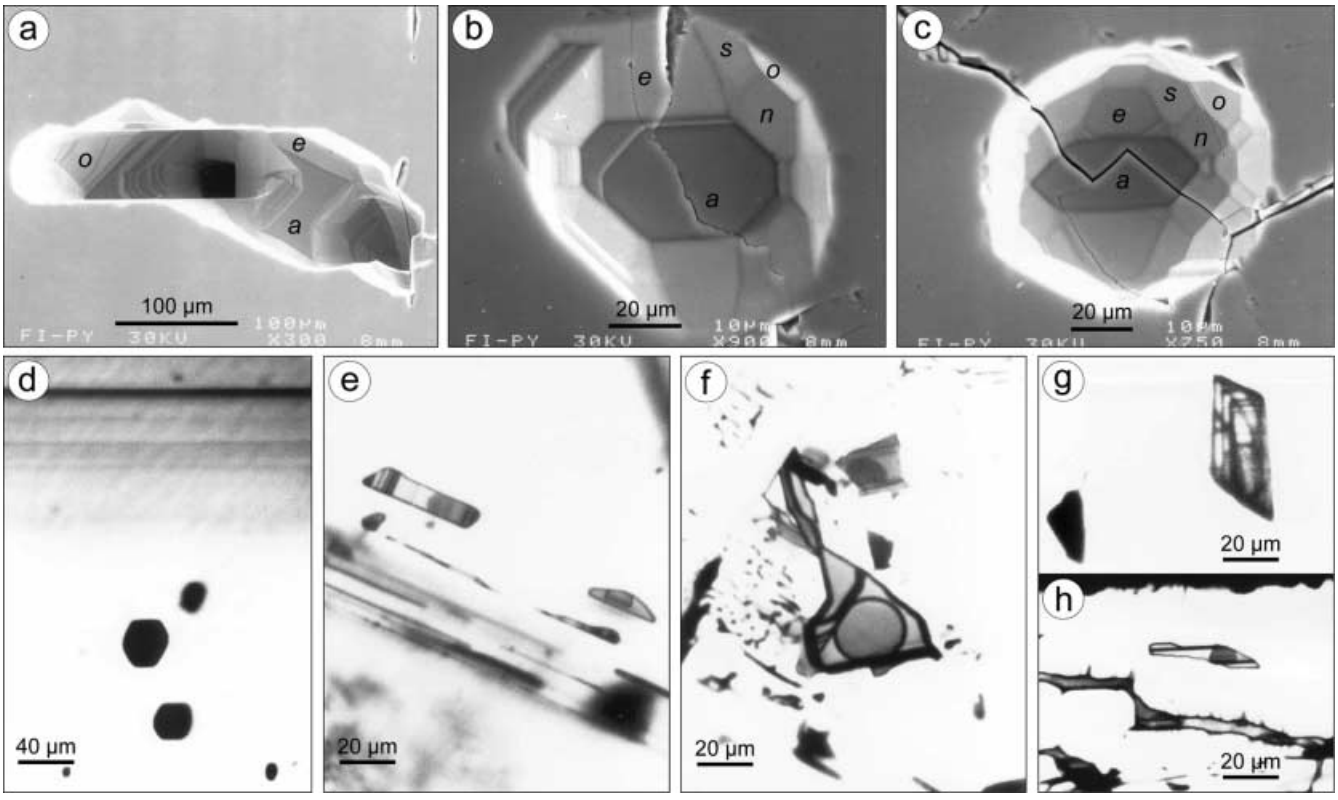

Fig. 5a–h Primary fluid inclusions in pyrite. **a–c** SEM microphotographs of open fluid inclusion cavities with negative crystal shapes in sections cut parallel to (100). Crystal face indexes are as follows: *a* {100}, *o* {111}, *e* {210}, *n* {112}, *s* {321}. **a** Channel-like inclusion. **b**, **c** Nearly isometric inclusions. **d–h** IR transmitted light microphotographs of primary inclusions in sections cut parallel to (100). **d** Isometric primary inclusions parallel to (100) growth zones. Note the opacity of inclusions. **e** Flat and tabular inclusions arranged along (100) growth zones. **f** Large flat inclusion in the central part of pyrite crystal. **g** Isolated primary inclusion with striated faces. **h** Isolated primary inclusion neighbouring a secondary inclusion plane, affected by post-entrapment re-equilibration. Note the visible microcracking of secondary inclusions

are still dominant, but additional forms also play an important role (see Fig. 5c). These inclusions are as much as 70 µm in diameter. In IR light, they are completely opaque because of their complicated negative crystal shape (Fig. 5d).

Only flat and tabular inclusions are transparent to IR light (Fig. 5e–h). They are bounded by *a*, *o* and *e*. The dominant form is the cube, and the majority has striated faces. They occur along growth zones (Fig. 5e, f) or as isolated large inclusions in the crystal cores (Fig. 5g, h). Primary inclusions with highly irregular morphologies (with preferred two-dimensional development perpendicular to the crystal growth direction) may indicate fast crystal growth rates.

Secondary inclusions (Fig. 6) occur along planes cutting growth zones (Fig. 3d). Pyrite displays indistinct {100} cleavage, which can result in conchoidal to uneven fractures (Gaines et al. 1997). Two types of narrow healed fractures were observed: relatively flat planes with a net-like structure (Fig. 6a), or convex ones similar to those noted by Lüders and Ziemann (1999) and formed by concentric whirls of inclusions (Fig. 6b). Secondary inclusions are either two-phase (with variable vapour to liquid ratios) or monophase (liquid-filled). Their morphology is highly variable, depending on the surface morphology of the healed fracture: flat, stepped or curved in its different parts. Fluid inclusions in fracture planes parallel to (100) are dominantly bounded by *a* and *o* (Fig. 6c), and rarely by *e* (Fig. 6d). Necking-down features are common in secondary fluid inclusion planes (Fig. 6d, e). Some textures observed before heating runs are indicative of partial decrepitation subsequent to formation (Fig. 6f). In these cases, the neighbouring primary inclusions were not affected by this process (Fig. 5h).

Microthermometry

Pyrite-hosted fluid inclusions

Freezing runs were performed before heating. During freezing, the IR transparency of pyrite did not change, and no clathrate nucleation was seen. Solids (ice) were not directly observed. The formation and melting of ice were identified by deformation or movement of the vapour bubble. Temperature cycling (Goldstein and Reynolds 1994) was routinely used during cryometric measurements. By contrast, the IR transparency of pyrite progressively decreased on heating above about 200 °C, as previously reported for pyrite by Mancano and Campbell (1995) and Lüders and Ziemann (1999). However, pyrite remained sufficiently IR-transparent for

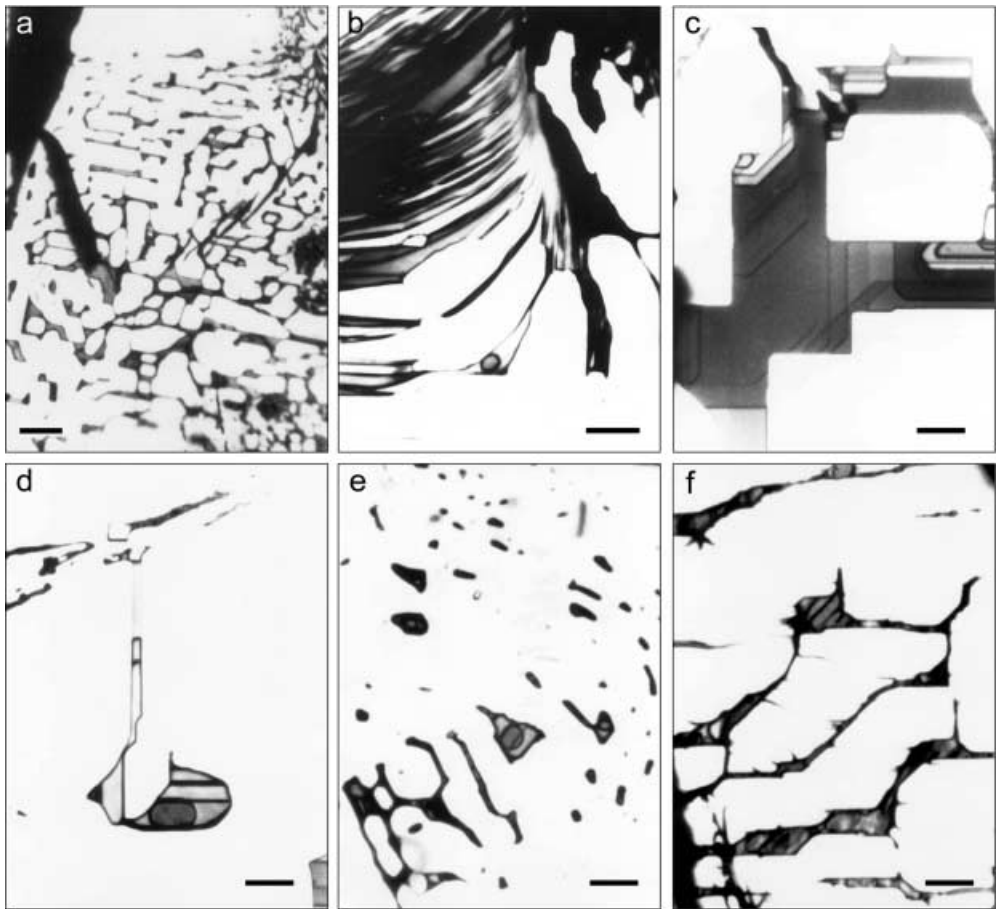

Fig. 6a–f IR transmitted light microphotographs of secondary fluid inclusions in pyrite. Sections cut parallel to (100). *Scale bar* 10 μm. **a** Net-like secondary fluid inclusion plane. **b** Convex secondary fluid inclusion plane. **c** Flat monophase inclusion bounded by {100} and {111}. **d** Typical texture of necking-down in secondary fluid inclusion. **e** Oblique plane of secondary inclusions. Note the different vapour/liquid ratios in different inclusions. **f** Secondary fluid inclusion with typical stretching textures

the measurements of the homogenisation temperature using the cycling technique. Reproducibility of melting and homogenisation temperature measurements are 0.1 and 1 °C, respectively.

Microthermometric results from pyrite-hosted fluid inclusions are illustrated on Fig. 7. Solidification of inclusion liquid occurred at ~–35/–40 °C. It was not possible to determine the first melting point in primary inclusions. For three inclusions, some changes were observed at temperatures ranging between –13.2 and –11.0 °C. The final melting points (Tm_{ice}) in primary inclusions range between –2.7 and –2.1 °C. For secondary inclusions, Tm_{ice} are between –3.8 and –0.8 °C (Fig. 7b). All inclusions homogenised to the liquid phase on heating. Homogenisation temperatures of primary inclusions are 327–365 °C and those of secondary inclusions lie between 217 and 356 °C (Fig. 7a). The large range for Th in secondary inclusions (Fig. 7c) is a result of necking-down processes.

Fluid inclusions in coexisting quartz

Fluid inclusions in quartz crystals from the late quartz–pyrite assemblage were also studied in order to compare microthermometric results between ore and gangue minerals. Quartz forms well-developed transparent crystals. Oriented sections, cut parallel and perpendicular to the *c*-axis, were used for the microscopic study. Growth zones of quartz crystals are defined by both fluid and solid inclusions (probably clay particles; Fig. 8a). Fluid inclusions in quartz are, therefore, primary (Fig. 8b). However, all primary inclusions have been naturally decrepitated, and some are cracked (Fig. 8b), whereas others were transformed to small fluid inclusion clusters (Fig. 8c). In the centre of each group, there is one liquid–vapour-filled inclusion, surrounded by a planar halo of very small liquid-filled inclusions (≤ 2–3 μm in size). No systematic microthermometric measurements were performed on such quartz-hosted fluid inclusions because of the obvious post-entrapment change in their primary morphologies. Cryometric measurements were performed on five inclusions only. Solidification of inclusion liquid occurs at –36/–38 °C. The final melting points of ice of five inclusions ranged from –2.6 to –2.5 °C.

Discussion

Pyrite chemistry and IR transmittance

The most common elements that can be incorporated into the pyrite lattice to form extensive solid solutions are As, Co and Ni. Conventional electron microprobe

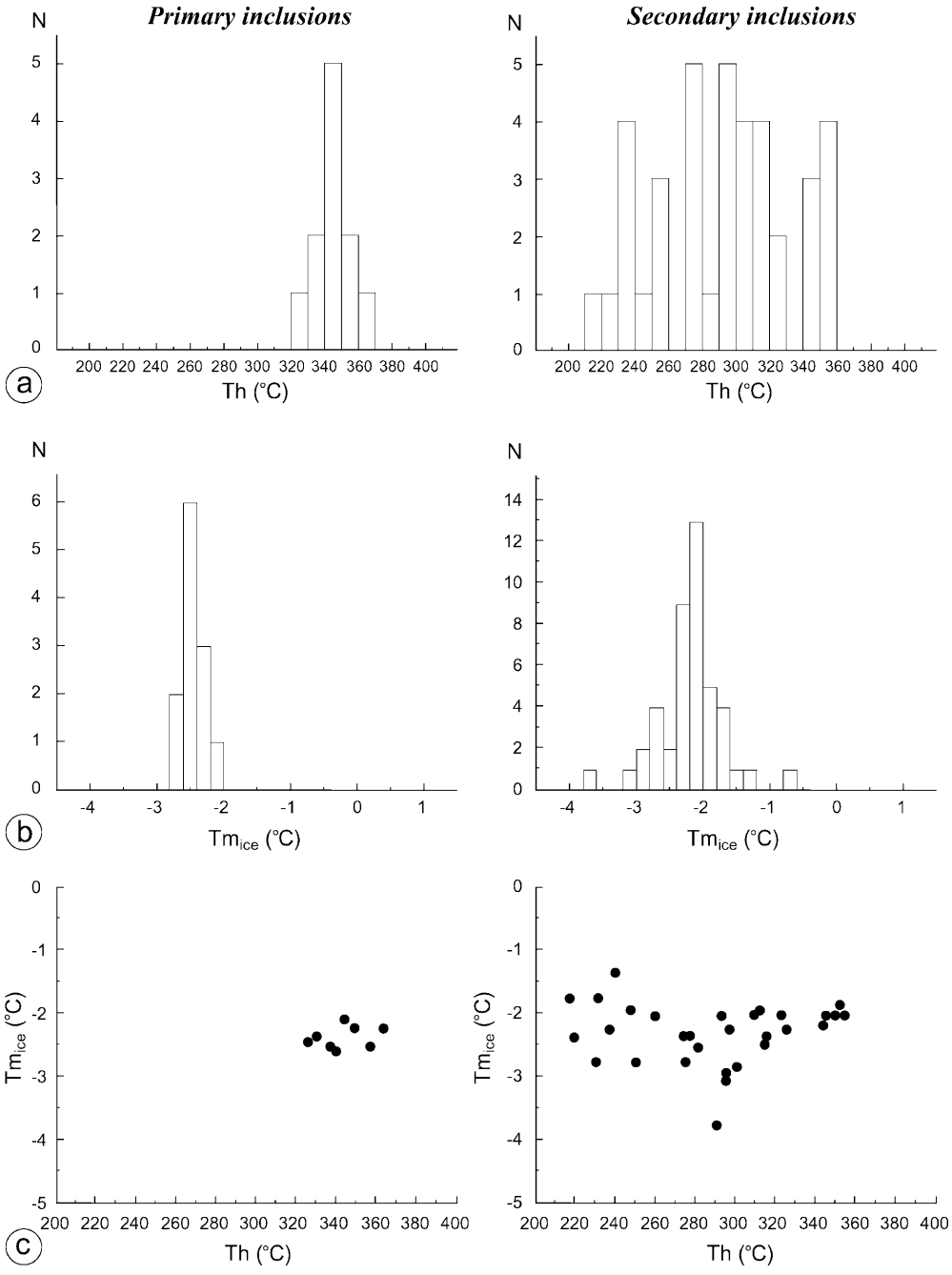

Fig. 7a–c Microthermometric data for primary and secondary fluid inclusions in pyrite from the Radka deposit (quartz–pyrite assemblage). **a** Temperatures of homogenisation. **b** Final ice melting temperatures. **c** Th vs. Tm_{ice} diagrams

analysis does not detect minor contents of these elements, but they can be detected and mapped with high beam currents, very long counting times and image enhancement (Craig et al. 1998). The IR transparency of pyrite appears to depend strongly on the trace element content (Kulis and Campbell 1999). Thus, the IR petrography and microspectroscopy have been used to study this phenomenon at Radka.

The early arsenian pyrite generation (pyrite–quartz assemblage) is completely opaque to IR radiation. This result is in good agreement with the previous conclusion by Richards and Kerrich (1993) stating that pyrite containing more than 0.5 wt% As is IR opaque. Cook and Chryssoullis (1990) showed that arsenic concentrations between 0.2 and 0.4 wt% are threshold values above which arsenic is incorporated into the pyrite structure. This, plus the fact that arsenic-free pyrite is IR transparent, may suggest that the incorporation of arsenic into the pyrite lattice causes its IR opacity. This interpretation, however, requires further experimental verification. The possibility that the IR opacity of the early Radka pyrite is caused by its colloform texture cannot be discarded. Fine-grained aggregates pre-determine the existence of numerous planes oblique to the section, corresponding to crystal faces, and these planes considerably decrease IR transparency.

The late, euhedral cobalt-bearing pyrite generation (late quartz–pyrite vein assemblage) exhibits a more

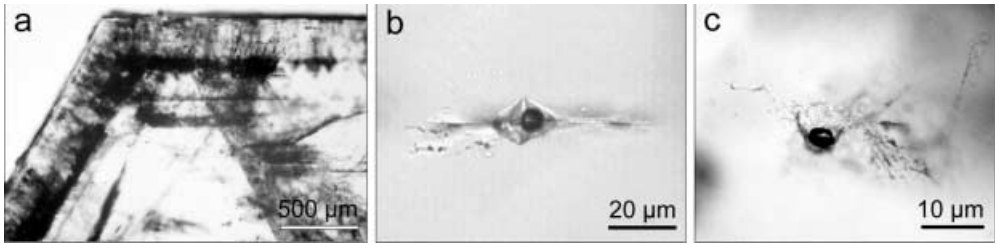

Fig. 8a–c Fluid inclusions in quartz. **a** Zoned quartz crystal cut perpendicular to c-axis. Growth zones are marked by fluid inclusions or solid inclusions of clay minerals. **b** 'Exploded' primary fluid inclusion parallel to the growth zone. **c** 'Decrepitation cluster' in the central part of the crystal

complex relationship between crystal zoning and IR transmittance. Microprobe analyses and X-ray elemental mapping demonstrate that the crystal banding observed under IR light results from variable cobalt contents (Figs. 3 and 4).

Compositional changes in naturally zoned crystals may have two main causes (Shore and Fowler 1996). Extrinsic mechanisms involve large-scale physical and chemical changes within the entire hydrothermal system (temperature, f_{O2}, fluid chemistry) that are partially or wholly independent of local crystallisation. Crystal growth can also be controlled solely by local, intrinsic phenomena, such as growth rate, solute diffusion through the crystal-fluid boundary layer, etc. Cyclic 'poisoning' by absorbed growth-inhibiting ions or the kinetics of attachment of end member units of solid solution (Ortoleva 1990) are other intrinsic mechanisms that allow for the development of zoned crystals.

Euhedral pyrite exhibits two different types of zoning visible on IR images and X-ray mapping. First, cobalt-enriched dark bands are visible at the crystal scale and they coincide with significant changes in the crystal habit (Figs. 3c and 4a). Second, the darker growth bands show very finely-banded internal oscillatory zoning, as is typical of arsenian pyrite (Fleet et al. 1989; Fig. 3b–d). Several tens of these fine zones can be identified within a single dark crystal band. Such large euhedral pyrite crystals with delicate banding have probably grown nearly in equilibrium with their parent solutions (Barton 1991). Thus, the larger scale zoning of euhedral pyrite could be related to physico-chemical changes in the hydrothermal environment. By contrast, the fine zoning probably results from intrinsic mechanisms, such as attachment of end member units of solid solution (in this case FeS_2 and CoS_2) or diffusion at the micrometre-scale through the boundary layer, although extrinsic controlling factors, cannot be excluded.

The measured IR transmittance spectra of pyrite (Fig. 3a) are very similar to those reported by Lüders and Ziemann (1999). The band gap energy for studied pyrite ranges from 0.91 to 0.89 eV, which corresponds to $\lambda = 1.36$–1.38 µm. Cobalt-free pyrite shows maximum transmittance at $\lambda = 1.7$ µm, corresponding to a quantum energy of 0.73 eV. The transmittance of cobalt-bearing growth bands is maximum at $\lambda = 1.56$ µm (0.79 eV) and rapidly decreases to zero at $\lambda = 1.9$ µm. The IR transmittance increases slightly at $\lambda > 2.15$ µm, and it reaches more significant values (as much as 20%) outside the spectral range of the IR-TV camera. The strong IR absorption for λ values between 1.9 and 2.1 µm is not an isolated phenomenon. It was previously identified by Lüders and Ziemann (1999) for pyrite samples of different origins (see Figs. 1 and 2 of their paper). Kulis and Campbell (1999) reported the same results. They mentioned theoretical calculations suggesting that the 2-µm absorption peak in pyrite is most likely caused by crystal-field transitions of low-spin Co^{2+} ions, which occur in a $Fe_{(1-x)}Co_xS_2$ solid solution as stoichiometric substitutions for Fe^{2+}.

The IR spectra collected on growth zones with different cobalt contents show that very small compositional changes of few hundred ppm Co, can cause a significant IR-transmittance decrease (as much as 80%; Fig. 3a, b). The fine zoning observed in Fig. 3b is probably caused by even smaller variations of cobalt (several tens of ppm Co), which are below EPMA detection limits. It was not possible to use IR spectroscopy to quantify the IR absorption in different fine zones because the aperture diameter of 20 µm used in this study mainly exceeds the width of growth zones.

We conclude that the IR absorption of pyrite strongly depends on the trace element concentrations and shows extreme variations in response to small compositional changes. Thus, IR spectrometry coupled with IR microscopy observations may be used to study qualitatively and to visualise small compositional changes, especially for such elements as arsenic and cobalt in pyrite, which in some cases are undetectable by standard analytical techniques.

Opacity and morphology of fluid inclusions

The opacity of some of the pyrite-hosted fluid inclusions (Fig. 5d) is attributed to a high refractive index contrast between pyrite and the trapped aqueous fluid (Richards and Kerrich 1993), resulting in intense refraction of light. Lüders and Ziemann (1999) suggested that post-entrapment reactions of the fluid with the host-mineral induced the precipitation of a solid phase on the inclusion walls, and this rim absorbs near-IR light and makes inclusions opaque.

In this present study, the negative crystal shape of some pyrite-hosted fluid inclusions was noted. Because pyrite is a cubic mineral, in some cases fluid inclusions have polyhedral morphology complicated by the presence of numerous small faces that are oblique to the IR beam (Fig. 5b, c). We argue that this complex morphology is the cause for the total internal light reflection, thus resulting in complete opacity of the fluid inclusion. There are numerous examples of negative crystal-shaped inclusions that are opaque to transmitted light, even in completely transparent minerals such as quartz (Roedder 1984) or iron-poor sphalerite (Bonev and Kouzmanov 1997). Our conclusion seems more probable for the studied pyrite from the Radka deposit, but it does not invalidate the interpretations proposed by Richards and Kerrich (1993) and Lüders and Ziemann (1999) for other samples. As predicted by Richards and Kerrich (1993), only oblate fluid inclusions lying flat in the plane of the section are transparent in IR light.

Fluid chemistry

In the absence of eutectic points and other phase transition measurements, similar solidification points and melting points of ice in fluid inclusions in quartz- and in most primary pyrite-hosted inclusions can be interpreted in terms of the H_2O–NaCl system, indicating salinities between 3.5 and 4.9 wt% equiv. NaCl (Bodnar 1993). In pyrite, ice crystals have never been clearly observed. Only vapour bubble movements have been observed, and these are interpreted as corresponding to the melting of solids. In three primary inclusions in pyrite, such movements were observed in the temperature range –13.2 to –11.0 °C (T_1' on Fig. 9) followed by the melting of ice at –2.3 to –2.1 °C (T_2' on Fig. 9). The measurements at ~–12 °C may correspond only to reorganisation of the melting ice crystals in the inclusion. However, similar cryometric data in pyrite were previously interpreted to correspond to eutectic points of KCl-rich solutions (Lüders and Ziemann 1999) because the eutectic point in the binary H_2O–KCl system is –10.7 °C (Hall et al. 1988). If the measured temperatures at ~–12 °C correspond to real phase transitions, they can be interpreted only in the H_2O–NaCl–KCl system, as corresponding to the melting of sylvite along the ice–sylvite cotectic (T_1'' in Fig. 9), before reaching the ice melting point (T_2''). If the observed transition is indeed sylvite dissolution, then the three measured data sets at –11/–2.1, –12.6/–2.3 and –13.2/–2.1 °C in Radka pyrites characterise inclusion fluids with bulk salinities of approximately 4.0–4.6 wt% and NaCl/(NaCl + KCl) wt. ratios of 0.05, 0.24 and 0.30, respectively (Bodnar et al. 1989). Such dominantly potassic fluids could tentatively be related to adularisation and sericitisation processes that accompany epithermal mineralisations in the Panagyurishte district (Chipchakova 1974). The later interpretation, however, remains speculative in the absence of direct identification of sylvite in the inclusions.

Thermobarometry

The Th of primary inclusions between 327 and 365 °C indicate high temperature deposition conditions for the late Radka pyrite, probably from magma-heated or even magmatic fluids. The maximum Th value of 365 °C measured in the late pyrite fixes a minimum pressure of 190 bar for pyrite deposition (Zhang and Frantz 1987). The fluid P–T–X conditions at Radka are quite similar to those described for many seafloor hydrothermal vent sites. Formation temperatures of 330–360 °C were proposed for the precipitation of sulphide minerals along the East Pacific Rise, based on direct temperature measurements (Tivey et al. 1990) and on the $^{40}Ar/^{4}He$ ratio of trapped fluids in sulphide minerals (Turner and Stuart 1992). A temperature of 400 °C represents the likely maximum for the late pyrite generation at Radka. This is because 400 °C is the upper limit for seawater-like fluid venting at ~250 bar seafloor conditions at mid-ocean ridges (Jupp and Schultz 2000), and such P–T–X conditions correspond to those at Radka. The trapping temperature of 400 °C applied to a fluid inclusion with Th = 365 °C can be used to estimate a maximum trapping pressure of about 430 bar in the Radka deposit (Zhang and Frantz 1987). This implies a maximum depth of ≈7 km under hydrostatic conditions and of ≈2 km under lithostatic conditions, taking into account a rock density of 2.35 (the density of altered dacitic volcanics at Radka: Kozhouharov and Iliev 1984). However, it is difficult to be more precise regarding the formation depth of the late pyrite because of the lack of precise knowledge of the fluid pressure regime.

Decrepitation of pyrite- and quartz-hosted inclusions

There are numerous geological and experimental observations showing that fluid inclusions trapped in a variety of minerals over a wide range of P–T conditions may re-equilibrate as a result of post-trapping P–T changes (Pécher and Boullier 1984; Lacazette 1990; Vityk and Bodnar 1995 and references therein) or deformation (Audétat and Günther 1999). Both the pyrite- and quartz-hosted fluid inclusions from Radka late-stage veins present textural evidences of re-equilibration. All quartz-hosted fluid inclusions have decrepitated as they display microcracks and are surrounded by planar arrays of tiny inclusions. The late Radka pyrite contains both unequilibrated inclusions (the primary and most secondary ones, see above) and some secondary inclusions that are affected by microcracking (Figs. 5h and 6f).

The observed brittle behaviour of the Radka pyrite near overpressured or under pressured fluid inclusions is consistent with the brittle to cataclastic behaviour of

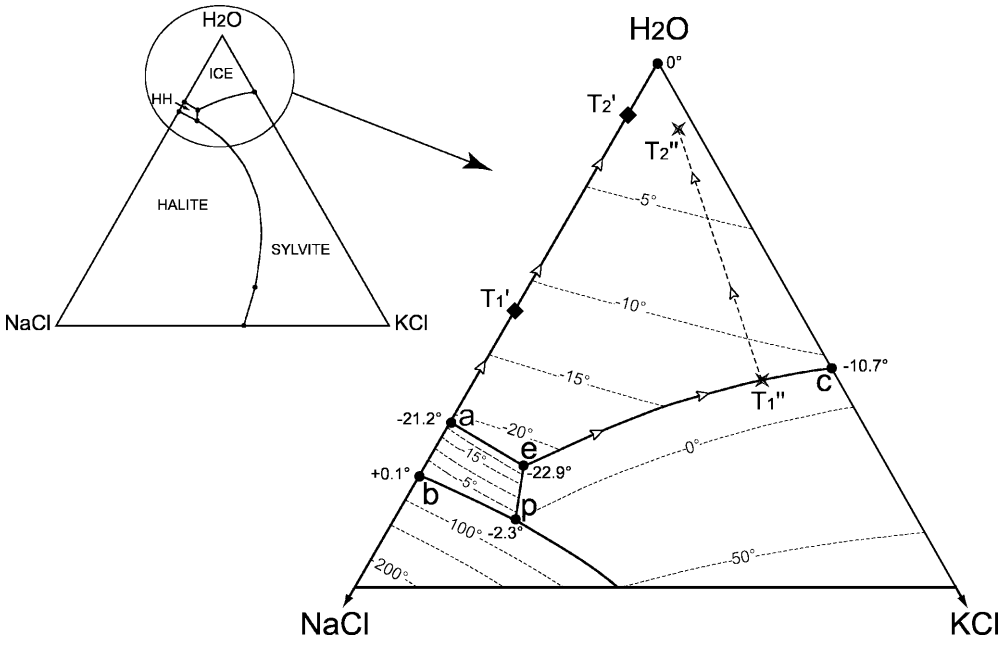

Fig. 9 Vapour-saturated solubility surface in the H_2O–NaCl–KCl system (after Sterner et al. 1988). The surface contains four stability fields – halite, sylvite, hydrohalite (NaCl $2H_2O$) and ice – each in equilibrium with liquid and vapour. The *heavy solid lines* separating the fields are cotectics representing the simultaneous stabilities of four phases. Points *a* and *c* are eutectics in the NaCl–H_2O and KCl–H_2O binary systems, respectively. Points *b* and *p* represent the peritectic compositions in the NaCl–H_2O binary, and NaCl–KCl–H_2O ternary systems, respectively. Point *e* is the ternary eutectic point at –22.9 °C. The possible paths of solid phase dissolution to interpret cryometric measurements in pyrite-hosted fluid inclusions are indicated by *small arrows*. See text for explanation

pyrite over a wide range of P and T (Graf and Skinner 1970). A specific feature of the Radka pyrite is that it shows partly decrepitated secondary fluid inclusions. In particular, the incompletely sealed fan-like crack shown on Fig. 5b (see also Fig. 3f in Lüders and Ziemann 1999) preserved the unstable, step-like propagation of a hydraulic fracture surrounding a point of concentrated stress. It probably corresponds to an intermediate stage of subcritical crack growth (Atkinson 1987). The contrasting behaviour of primary inclusions in the late pyrite can readily be explained by growth conditions at near-critical temperature. Only the primary inclusions that have trapped the hottest least compressible fluid are relatively insensitive to stretching. All primary inclusions that trapped a cooler fluid have probably decrepitated and reorganised into planar arrays, as they were submitted to drastic post-entrapment changes along steeper isochores.

Based on an elastic mechanical approach of fluid inclusion decrepitation (Lacazette 1990), quartz- and pyrite-hosted fluid inclusions should display a similar tendency to decrepitate, as they have near identical stress intensity resistance factors (Atkinson 1987). This conclusion may have to be revised (see also discussion by Audétat and Günther 1999) or, more likely, the fact that all primary quartz-hosted fluid inclusions have decrepitated may indicate that quartz started to precipitate at lower temperatures than pyrite.

The nature of the post-trapping P–T change that caused the decrepitation of quartz- and pyrite-hosted inclusions from the late Radka vein stage can be further discussed, when taking into account the maximum formation pressure of 430 bar. Also, a minimum differential pressure of 1.0–1.5 kbar will be considered as required to have initiated decrepitation in pyrite, by analogy with quartz and considering that the diameters of pyrite-hosted inclusions range between 5 and 50 μm (Lacazette 1990; see above). In the low-pressure volcanogenic environment prevailing at Radka, isobaric heating is the only likely phenomenon that can have provoked the inclusion decrepitation.

If we interpret primary decrepitated inclusions in pyrite as having maximum Th of approximately 330 °C, then it implies that the internal overpressure in such inclusions with Th = 330 °C reached ≈1.0–1.5 kbar during the reheating process. This fixes the temperature of the reheating at Radka at 500–550 °C (Zhang and Frantz 1987). The presence of secondary decrepitated inclusions with Th < 330 °C in both quartz and pyrite suggests that a second hydrothermal event pre-dated the reheating. Also, the existence of undecrepitated secondary inclusions with Th < 330 °C in pyrite shows that a late hydrothermal event affected this mineral subsequent to the reheating.

Fluid evolution at the Radka deposit

Despite the presence of rare gangue minerals such as quartz, barite, calcite and anhydrite at Radka, no systematic study of fluid inclusions was possible because of the fine-grained and/or cryptocrystalline character of their aggregates. According to Strashimirov and

Kovachev (1992), the early pyrite–quartz paragenesis at Radka precipitated at 225–245 °C; unfortunately no data about fluid salinities are available. The following main copper-bearing stage was formed at slightly higher temperatures (Th = 220–260 °C, corresponding to minimum trapping temperatures) from low salinity fluids (2.4–3.4 wt% equiv. NaCl; Kouzmanov et al. 2000b). There are no data for the intermediate (enargite–pyrite, bornite–tennantite and sphalerite–galena) stages. Fluid inclusions in the late cobalt-bearing quartz–pyrite assemblage studied here give evidence of a slight increase of the salinity of ore-forming solutions (to a maximum bulk value of 4.6wt%) and for mineral precipitation at significantly higher temperatures (maximum estimated trapping temperature of ~400 °C). The later anhydrite assemblage was formed by cooler fluids at 230–180 °C (Strashimirov and Kovachev 1992). A possible explanation of this evolution at Radka is the contribution to the hydrothermal system during the late quartz–pyrite stage of magmatic fluids, which resulted in increasing temperature and salinity of the solutions. Sulphur isotopic data ($\delta^{34}S \approx 0‰$) for the late cobalt-bearing pyrite (Kouzmanov and Lerouge, unpublished data) are in agreement with such a hypothesis. This could indicate pulses of magmatic low-salinity vapour ascending from and condensing above a deeper porphyry copper system, after the formation of the main Cu–As (± Au) stage (Heinrich et al. 1999).

Metallogenic implications

This study provides the first description of fluids that deposited cobalt-bearing pyrite in a replacement epithermal deposit in the Panagyurishte district. Rare occurrences of Co- and Ni-bearing minerals have been described in the porphyry-copper deposits of the district (Strashimirov et al. 2002, this volume): carrollite and Co- and Ni-bearing pyrites from the Medet porphyry copper (Strashimirov 1982); cobaltite, linnaeite and millerite from the Tsar Assen porphyry copper (Bogdanov and Bogdanova 1978), and siegenite and bravoite from the Assarel porphyry copper deposit (Bogdanov 1987). Thiospinels with dominant carrollite–cuprian siegenite and nickeloan siegenite compositions were also found in the Elatsite porphyry copper deposit, located about 40 km north of Panagyurishte (Dragov and Petrunov 1998).

In porphyry copper deposits, cobalt-rich mineral assemblages (quartz–magnetite–bornite chalcopyrite and quartz–pyrite-chalcopyrite) are formed early in the ore paragenesis (Strashimirov et al. 2002, this volume). Fluid inclusion study of quartz from these assemblages provides evidence of the high-temperature and high-salinity character of fluids involved in the initial stages of hydrothermal activity in these porphyry copper systems (Strashimirov et al. 2002, this volume).

Comparing the mineralogy and fluid inclusion data of the late stage, cobalt-bearing, quartz–pyrite vein assemblage in the Radka deposit to those in typical porphyry copper systems (especially the quartz–pyrite–chalcopyrite assemblage) from the Panagyurishte district, we can consider the studied cobalt-bearing veins at Radka as the shallow manifestation of porphyry copper mineralisation at a depth of 2 km. The massive pyrite and copper-pyrite bodies have characteristic features of epithermal replacement type deposits of high- to intermediate-sulphidation style (Sillitoe 1983; Hedenquist 2000). This interpretation is compatible with the cogenetic development of the epithermal and porphyry ore deposits within the volcano-plutonic complexes, which is typical of magmatic arc environments (Sillitoe 1980, 1983; Marcoux 1995; Hedenquist et al. 1998).

Conclusions

The systematic study of crystal zoning, composition, IR transmittance, IR petrography and microthermometry of pyrite samples from the Radka copper deposit shows evidence for two distinct pyrite generations based on their textures, structures, composition and behaviour in IR light. The early and late pyrite generations are chemically zoned in arsenic and cobalt, respectively. There is a negative correlation between trace-element content and IR transmittance of pyrite. The IR transparency of pyrite is a very sensitive indicator for changes of trace element concentration: several hundreds of ppm Co result in an important decrease of IR transmittance (as much as 80%). Arsenic-bearing pyrite (≤ 2.2 wt% As) is completely opaque to IR radiation.

A characteristic feature of primary fluid inclusions in pyrite is the negative crystal habit, shaped mainly by {100}, {111} and {210}. This complicated polyhedral morphology is the reason for the observed opacity of some isometric primary inclusions. Secondary fluid inclusion morphology depends on the nature of the surface of the healed fracture. Recognition of primary or secondary origin of fluid inclusions is greatly enhanced by using crystallographically oriented sections. Microthermometric data from primary inclusions indicate that the late pyrite generation was deposited at maximum P–T conditions of 400 °C and 430 bar and from a fluid of low bulk salinity (3.5–4.6 wt%), possibly KCl-dominant. We conclude that the late, moderate-temperature, cobalt-bearing quartz–pyrite vein assemblage in the Radka deposit is the shallow (≤ 2 km) manifestation of porphyry copper mineralisation at depth, in agreement with an epithermal replacement origin of orebodies. Decrepitation of quartz- and pyrite-hosted fluid inclusions is consistent with reheating of the late veins to 500–550 °C in relation to a magmatic source of heat.

Acknowledgements We thank Volker Lüders, Ivan Bonev, Rumen Petrunov, Robert Moritz and Thomas Kerestedjian for discussions. We much appreciate the careful review by Jeffrey Hedenquist,

which resulted in substantial improvements of the manuscript. We are indebted to Jeremy Richards and Robert Moritz for their helpful comments and their critical reviews. The final version of the manuscript was revised according to helpful comments of Richard Goldfarb and Chris Heinrich. This is a contribution to the GEODE (European Science Foundation) programme 'Geodynamics and ore deposit evolution of the Alpine–Balkan–Carpathian–Dinaride Province'.

References

Andrew CJ (1997) The geology and genesis of the Chelopech Au–Cu deposit, Bulgaria: Europe's largest gold resource. In: Europe's Major Gold deposits Conference, Newcastle, North Ireland, Abstr vol and program, pp 68–72

Atkinson BK (1987) Fracture mechanics of rocks. Academic Press, London

Audétat A, Günther D (1999) Mobility and H_2O loss from fluid inclusions in natural quartz crystals. Contrib Mineral Petrol 137:1–14

Bailly L (1998) Etude par microscopie infrarouge des inclusions fluides piégées dans les minéraux opaques. Bureau de Recherches Géologiques et Minières (BRGM) Report no. 40209

Bailly L, Bouchot V, Bény C, Milési J-P (2000) Fluid inclusion study of stibnite using infrared microscopy: an example from the Brouzils antimony deposit (Vendée, Armorican massif, France). Econ Geol 95:221–226

Barton PB Jr (1991) Ore textures: problems and opportunities. Mineral Mag 55:303–315

Bodnar RJ (1993) Revised equation and table for determining the freezing point depression of H_2O–NaCl solutions. Geochim Cosmochim Acta 57:683–684

Bodnar RJ, Sterner SM, Hall DL (1989) SALTY: a Fortran program to calculate compositions of fluid inclusions in the system NaCl–KCl–H_2O. Computers Geosci 15:19–41

Bogdanov B (1980) Massive sulphide and porphyry copper deposits in the Panagjurishte district, Bulgaria. In: Jankovic S, Sillitoe RH (eds) European copper deposits. Society for Geology Applied to Mineral Deposits (SGA), Belgrade, Special Publ no 1, pp 50–58

Bogdanov B (1984) Hydrothermal systems of massive sulphide, porphyry-copper and vein copper deposits of Sredna Gora zone in Bulgaria. Proceedings of the Sixth Quadrennial International Association of the Genesis of Ore Deposits Symposium, Stuttgart, pp 63–67

Bogdanov B (1987) Copper deposits in Bulgaria (in Bulgarian). Technika, Sofia

Bogdanov B, Bogdanova R (1974) The Radka copper-pyrite deposit. In: Dragov P, Kolkovski B (eds) Twelve ore deposits of Bulgaria. IV Symposium of the International Association of the Genesis of Ore Deposits, Varna, pp 114–133

Bogdanov B, Bogdanova R (1978) Mineral parageneses in primary ores from the Tsar Assen deposit (in Bulgarian). In: Velchev V (ed) 25 years of the Higher Institute of Mining and Geology, Sofia, pp 26–32

Bonev I, Kouzmanov K (1997) Fluid inclusions in sphalerite as negative crystals. In: Boiron MC, Pironon J (eds) Proc XIV ECROFI Volume de Résumés, Nancy, pp 50–51

Bonev IK, Kerestedjian T, Atanassova R, Andrew CJ (2002) Morphogenesis and composition of native gold in the Chelopech volcanic-hosted Au–Cu epithermal deposit, Srednogorie zone, Bulgaria. Miner Deposita (in press). DOI 10.1007/s00126-002-0273-8

Campbell AR, Panter KS (1990) Comparison of fluid inclusions in coexisting (cogenetic?) wolframite, cassiterite, and quartz from St Michael's Mount and Cligga Head, Cornwall, England. Geochim Cosmochim Acta 54:673–681

Campbell AR, Robinson-Cook S (1987) Infrared fluid inclusion microthermometry on coexisting wolframite and quartz. Econ Geol 82:1640–1645

Campbell AR, Hackbarth CJ, Plumlee GS, Petersen U (1984) Internal features of ore minerals seen with the infrared microscope. Econ Geol 79:1387–1392

Campbell AR, Robinson-Cook S, Amindyas C (1988) Observation of fluid inclusions in wolframite from Panasqueira, Portugal. Bull Minéral 111:251–256

Chipchakova S (1974) Adularization in the altered volcanics around the ore bodies of the Panagyurishte ore district, Bulgaria. Bull Volcanologique 38:1147–1156

Chipchakova S, Karadjova B, Andreev A, Stefanov D (1981) Rare alkalis in wall-rock metasomatites of massive copper-pyrite deposits in Central Srednogorie, Bulgaria. Geol Balkanica 11:89–102

Cook N, Chryssoulis S (1990) Concentrations of 'invisible gold' in the common sulfides. Can Mineral 28:1–16

Craig JR, Vokes FM, Solberg TN (1998) Pyrite: physical and chemical textures. Miner Deposita 34:82–101

Dimitrov C (1960) Magmatismus und Erzbildung im Erzgebiet von Panagjuriste. Freiberg Forschungshefte C 79:67–81

Dowty E (1989) SHAPE: a computer program for drawing crystals. IBM-PC version 3.1. Instruction Manual, Kingsport

Dragov P, Petrunov R (1998) Compositions of thiospinel minerals from the Elatsite porphyry-copper deposit (in Bulgarian with English abstract). Geochem Mineral Petrol 33:25–28

Fleet ME, Mumin AH (1997) Gold-bearing pyrite and marcasite and arsenopyrite from Carlin Trend gold deposits and laboratory synthesis. Am Mineral 82:182–193

Fleet ME, Maclean PJ, Barbier J (1989) Oscillatory-zoned As-bearing pyrite from strata-bound and stratiform gold deposits: an indicator of ore fluid evolution. The geology of gold deposits: the perspective in 1988. Econ Geol Monogr 6:356–362

Fleet ME, Chryssoulis SL, Maclean PJ, Davidson R, Weisener CG (1993) Arsenian pyrite from gold deposits: Au ands As distribution investigated by SIMS and EMP, and color staining and surface oxidation by XPS and LIMS. Can Mineral 31:1–17

Gaines RV, Skinner HCW, Foord EE, Mason B, Rosenzweig A (1997) Dana's new mineralogy: the system of mineralogy of James Dwight Dana and Edward Salisburg Dana, 8th edn. Wiley, New York

Goldstein R, Reynolds T (1994) Systematics of fluid inclusions in diagenetic minerals. Society for Sedimentary Geology short course 31

Graf JL, Skinner BJ (1970) Strength and deformation of pyrite and pyrrhotite. Econ Geol 65:206–215

Hall DL, Sterner SM, Bodnar RJ (1988) Freezing point depression of NaCl–KCl–H_2O solutions. Econ Geol 83:197–202

Heald P, Foley NK, Hayba DO (1987) Comparative anatomy of volcanic-hosted epithermal deposits: acid-sulfate and adularia–sericite types. Econ Geol 82:1–26

Hedenquist JW (2000) The magmatic to epithermal continuum: Present understanding, new ideas, and critical questions. In: ABCD–GEODE 2000 Workshop, Borovets, Bulgaria, Abstracts

Hedenquist JW, Arribas A Jr (1999) Epithermal gold deposits: I. Hydrothermal processes in intrusion-related systems, and II. Characteristics, examples and origin of epithermal gold deposits. In: Molnar F, Lexa J, Hedenquist JW (eds) Epithermal mineralization of the western Carpathians. Society of Economic Geologists guidebook series 31, pp 13–63

Hedenquist JW, Lowenstern JB (1994) The role of magmas in the formation of hydrothermal ore deposits. Nature 370:519–527

Hedenquist JW, Arribas A Jr, Reynolds TJ (1998) Evolution of an intrusion-centered hydrothermal system: Far Southeast-Lepanto porphyry and epithermal Cu–Au deposits, Philippines. Econ Geol 93:373–404

Heinrich CA, Günther D, Audétat A, Ulrich T, Frischknecht R (1999) Metal fractionation between magmatic brine and vapor, determined by microanalysis of fluid inclusions. Geology 27:755–758

Herzig PM, Hannington MD, Arribas A (1998) Sulfur isotopic composition of hydrothermal precipitates from the Lau

back-arc: implications for magmatic contributions to seafloor hydrothermal system. Miner Deposita 33:226–237
Jupp T, Schultz A (2000) A thermodynamic explanation for black smoker temperatures. Nature 403:880–883
Kouzmanov K, Bogdanov K, Ramboz C (2000a) Cu–Bi–Pb–Te mineral assemblage in the Elshitsa and Radka deposits, Sredna Gora zone, Bulgaria. In: ABCD-GEODE 2000 Workshop, Borovets, Bulgaria, Abstracts
Kouzmanov K, Bény J-M, Ramboz C, Bailly L (2000b) CO_2–H_2, sericite- and kaolinite-bearing fluid inclusions from the Radka copper deposit, Sredna Gora zone, Bulgaria – evidence for advanced argillic alteration. In: ABCD-GEODE 2000 Workshop, Borovets, Bulgaria, Abstracts
Kouzmanov K, Moritz R, Chiaradia M, Fontignie D, Ramboz C (2001) Sr and Pb isotope study of Au–Cu epithermal and porphyry-Cu deposits from the southern part of the Panagyurishte district, Sredna Gora zone, Bulgaria. In: Piestrzynski et al. (eds.) Mineral deposits at the beginning of the 21st century. Proceedings of the joint 6th biennial SGA-SEG meeting, Krakow, Poland, 26–29 August, pp 539–542
Kozhouharov E, Iliev Z (1984) Petrophysical investigations of the rocks from the Radka volcanogenic strip (in Bulgarian). Ann Univ Sofia 'St Kliment Ohridski' Facult Géol Géogr Livre 1 89:122–137
Kulis J, Campbell A (1999) Cobalt control on near-infrared transparency of pyrite. Geol Soc Am Abstr Programs 31(7):170
Lacazette A (1990) Application of linear elastic fracture mechanics to the quantitative evaluation of fluid-inclusion decrepitation. Geology 18:782–785
Lüders V (1996) Contribution of infrared microscopy to fluid inclusion studies in some opaque minerals (wolframite, stibnite, bournonite): metallogenic implications. Econ Geol 91:1462–1468
Lüders V, Ziemann M (1999) Possibilities and limits of infrared light microthermometry applied to studies of pyrite-hosted fluid inclusions. Chem Geol 154:169–178
Lüders V, Gutzmer J, Beukes N (1999) Fluid inclusion studies in cogenetic hematite, hausmannite, and gangue minerals from high-grade manganese ores in the Kalahari manganese field, South Africa. Econ Geol 94:589–595
Mancano DP, Campbell AR (1995) Microthermometry of enargite-hosted fluid inclusions from the Lepanto, Philippines, high-sulfidation Cu–Au deposit. Geochim Cosmochim Acta 59:3909–3916
Marcoux E (1995) Gold and volcanoes: epithermal gold deposits, a review. CR Acad Sci Paris 321, Ser II a:723–735
Milev VR, Stanev VB, Ivanov VH (1996) Statistical manual of the ore production in Bulgaria during 1878–1995 (in Bulgarian). Zemia 99 Publishing House, Sofia
Obretenov N, Popov P (1973) Structure of the Radkino ore field (in Bulgarian with English abstract). Bull Geol Inst, Metall Non-Metall Deposits Ser BAS 22:5–18
Ortoleva PJ (1990) Role of attachment kinetic feedback in the oscillatory zoning of crystals grown from melts. Earth-Sci Rev 29:3–8
Pécher A, Boullier A-M (1984) Evolution à pression et température élevées d'inclusions fluides dans un quartz synthétique. Bull Minéral 107:139–153
Popov P, Popov K (1997) Metallogeny of Panagyurishte ore region. In: Romic K, Konzulovic R (eds) Symposium 'Ore deposits exploration', Proceedings, Belgrade, 2–4 April 1997, pp 327–338
Pouchou JL, Pichouar F (1984) Un nouveau modèle de calcul pour la microanalyse quantitative par spectrométrie de rayons X. Partie I: Application à l'analyse d'échantillons homogènes. Rech Aérospatiale 3:167–192
Radonova T (1962) Primary mineralisation and wall-rock alterations in the area of Radka mine, in the vicinity of Panagiurishte (in Bulgarian with English abstract). Trav Géol Bulg, Sér Géochim Gîtes Metall Non-Metall 3:93–128
Ramdohr P (1981) The ore minerals and their intergrowths. Pergamon Press, Oxford
Richards JP, Kerrich R (1993) Observations of zoning and fluid inclusions in pyrite using a transmitted infrared light microscope ($\lambda \leq 1.9$ μm). Econ Geol 88:716–723
Roedder E (1984) Fluid inclusions. Mineral Soc Am, Rev Mineral, vol 12
Shore M, Fowler AD (1996) Oscillatory zoning in minerals: a common phenomenon. Can Mineral 34:1111–1126
Sillitoe RH (1980) The Carpathian–Balkan porphyry copper belt – a Cordilleran perspective. In: Jankovic S, Sillitoe RH (eds) European copper deposits. Society for Geology Applied to Mineral Deposits (SGA), Belgrade, Spec Publ no 1, pp 26–35
Sillitoe RH (1983) Enargite-bearing massive sulfide deposits high in porphyry copper systems. Econ Geol 78:348–352
Simon G, Kesler SE, Chryssoulis S (1999) Geochemistry and textures of gold-bearing arsenian pyrite, Twin Creeks, Nevada: implications for deposition of gold in Carlin-type deposits. Econ Geol 94:405–422
Sterner SM, Hall DL, Bodnar RJ (1988) Synthetic fluid inclusions. V. Solubility relations in the system NaCl–KCl–H_2O under vapour-saturated conditions. Geochim Cosmochim Acta 52:989–1005
Strashimirov S (1982) Cobalt-pyrite, nickel-pyrite and carrollite from the molybdenum–copper deposit Medet (in Bulgarian with English abstract). Rev Bulg Geol Soc 43:117–127
Strashimirov S, Kovachev V (1992) Temperatures of ore-formation in copper deposits from the Srednogorie zone based on fluid inclusion studies of minerals (in Bulgarian with English abstract). Rev Bulg Geol Soc 53:1–12
Strashimirov S, Petrunov R, Kanazirski M (2002) Porphyry copper mineralisations of the Central Srednogorie zone, Bulgaria. Miner Deposita (in press) DOI 10.1007/s00126-002-0275-6
Tivey MK, Olson LO, Miller VW, Light RD (1990) Temperature measurements during initiation and growth of a black smoker chimney. Nature 346:51–54
Tsonev D, Bogdanov B, Popov K (2000a) The volcanic-hosted sulphide (VHS) deposits from the southern part of the Panagyurishte ore region, Bulgaria. In: ABCD-GEODE 2000 Workshop, Borovets, Bulgaria, Abstracts
Tsonev D, Popov K, Kanazirski M, Strashimirov S (2000b) Radka ore field. In: Strashimirov S, Popov P (eds) Geology and metallogeny of the Panagyurishte ore region (Srednogorie zone, Bulgaria). ABCD–GEODE 2000 workshop, guidebook to excursions (A and C), pp 32–39
Tzonev D (1974) Evolution of the mineral parageneses in the Radka and Elshitsa cupriferous-pyritic deposits, Panagyurishte ore district, Bulgaria. In: Bogdanov B (ed) Problems of ore deposition. IV International Association of the Genesis of Ore Deposits Symposium, Varna, vol 2, pp 327–33
Tzonev D (1982) Radka copper-pyrite–polymetallic deposit. In: Vassileff L, Tzonev D, Bonev I (eds) 13th International Mineralogical Association Meeting, Varna, Guidebook 2 – Central Srednogorie, pp 23–36
Turner G, Stuart F (1992) Helium/heat ratios and deposition temperatures of sulphides from the ocean floor. Nature 357:581–583
Vityk MO, Bodnar RJ (1995) Textural evolution of synthetic fluid inclusions in quartz during reequilibration, with application to tectonic reconstruction. Contrib Mineral Petrol 121:309–323
Zhang YG, Frantz JD (1987) Determination of the homogenisation temperatures and densities of supercritical fluids in the system NaCl–KCl–H_2O using synthetic fluid inclusions. Chem Geol 64:335–350